

## Article

# Study on Mechanical Properties and Microstructural Evolution of Composite Copper Foils Following Long-Term Storage

Yujie Yan <sup>1</sup>, Haibo Chen <sup>1</sup>, Hang Li <sup>1</sup>, Jing Hu <sup>1</sup>, Ziye Xue <sup>2</sup>, Jianli Zhang <sup>1</sup>, Qiang Chen <sup>1</sup>, Guangya Hou <sup>1</sup>  and Yiping Tang <sup>1,\*</sup> 

<sup>1</sup> College of Materials Science and Engineering, Zhejiang University of Technology, Hangzhou 310014, China; 201806021425@zjut.edu.cn (Y.Y.); 201806021102@zjut.edu.cn (H.C.); 221122250270@zjut.edu.cn (H.L.); 211122250060@zjut.edu.cn (J.H.); zhangjianli@zjut.edu.cn (J.Z.); cq415@zjut.edu.cn (Q.C.); houguangya@zjut.edu.cn (G.H.)

<sup>2</sup> Zhejiang Gpilot Technology Co., Ltd., Wenzhou 325699, China; jeff@cnjiabo.com

\* Correspondence: tangyiping@zjut.edu.cn

**Abstract:** Composite copper foil, a novel negative electrode current collector developed in recent years, can significantly enhance battery safety and energy density while also conserving metallic resources. It is found that after 9 months of long-term storage, the tensile strength of the composite copper foil decreases by 9.76%, and the elongation rate drops by 26.32%. The internal texture of the composite copper foil shifts from a highly oriented (111) plane to a more random crystal plane orientation and the bonding strength is significantly improved. The study reveals that the residual stress within the copper layer provides the driving force for the changes in the microstructure; the intermediate PET layer plays a buffering and absorbing role in the stress-release process. It regulates the redistribution of stress, promoting the alteration of the copper layer's texture and the refinement of grains.

**Keywords:** composite copper foil; long-term storage; mechanical properties; texture shift; residual stress; role of PET



Academic Editor: George Zheng Chen

Received: 6 March 2025

Revised: 14 April 2025

Accepted: 23 April 2025

Published: 25 April 2025

**Citation:** Yan, Y.; Chen, H.; Li, H.; Hu, J.; Xue, Z.; Zhang, J.; Chen, Q.; Hou, G.; Tang, Y. Study on Mechanical Properties and Microstructural Evolution of Composite Copper Foils Following Long-Term Storage. *Batteries* **2025**, *11*, 173. <https://doi.org/10.3390/batteries11050173>

**Copyright:** © 2025 by the authors. Licensee MDPI, Basel, Switzerland. This article is an open access article distributed under the terms and conditions of the Creative Commons Attribution (CC BY) license (<https://creativecommons.org/licenses/by/4.0/>).

## 1. Introduction

Lithium-ion batteries, as the foremost energy storage and conversion devices in modern society, require synergistic improvement of energy density and safety performance, which has become a research focus in the new energy field [1–3]. Current collectors, serving as key functional components for electron transport and mechanical support inside the batteries, demonstrate performance evolution that directly impacts battery functionality and long-term reliability [4–6]. In the field of negative electrode current collectors, traditional electrolytic copper foils dominate due to their excellent conductivity and mature production technology. However, their thickness limitation ( $\geq 5 \mu\text{m}$ ) and low fracture elongation (typically required  $\geq 3\%$ ) fail to meet the dual demands of lightweighting and high security for high-specific-energy batteries [7–9].

In recent years, composite current collectors, employing a “metal-polymer-metal” sandwich-structured design, have demonstrated remarkable improvements in breaking through the bottleneck of lightweight (areal density reduced by 40–60%) while significantly enhancing nail penetration safety (thermal runaway triggering time delayed by  $\geq 300\%$ ) [10]. Composite copper foils typically utilize magnetron sputtering-electrochemical deposition processes to construct micron-scale copper layers on polymer substrates such as polyethylene terephthalate (PET). Owing to their special material composition and

sandwich architecture, composite copper foils exhibit superior enhancements in lithium battery safety, energy density, and cost-effectiveness compared to traditional electrolytic copper foils [11–13]. The adoption of polymer films substantially reduces foil weight, enhancing a 5–10% increase in battery specific energy ( $\text{Wh}\cdot\text{kg}^{-1}$ ). Polymer substrates exhibit superior plasticity, with fracture elongation (>30%) far exceeding that of electrolytic copper foils, effectively suppressing internal short-circuit propagation during nail penetration and mitigating electrode stress during cycling, thereby significantly improving battery safety [14,15]. Currently, composite copper foil technology has gradually achieved industrialization, with companies such as Sterio, Chongqing JMEV, and Rouzhen Technology achieving mass production. These products have been adopted by downstream battery customers, including CATL’s CTP 3.0 and GAC Aion’s Magazine Battery 2.0.

Traditional electrolytic copper foils exhibit a 42% reduction in tensile strength after 36 h of room temperature storage due to decomposition of residual organic additives from the electrodeposition process and grain self-annealing (or recrystallization) effects [16]. The copper layers in composite copper foils, also fabricated via electrodeposition, are subject to similar self-annealing effects, potentially leading to performance degradation during storage. Not enough attention has been paid to this phenomenon. Meanwhile, multiple material interfaces in composite foils may induce similar plating warpage debonding [17], while viscoelastic relaxation of PET substrates could exacerbate interfacial mechanical mismatch [18], and chemical oxidation at copper/polymer interfaces might initiate crack sprouting [19]. These latent risks directly affect structural integrity during winding processes, electrolyte infiltration, and electrochemical cycling. Current research on composite current collectors predominantly focuses on manufacturing optimization (e.g., gradient sputtering parameter design [20]) and initial performance characterization (e.g., cycling expansion rate test [21]), leaving systematic investigations into long-term storage stability and microstructural evolution absent. In commercial lithium battery production, current collector materials may undergo 3–6 months of storage and logistics cycles, during which performance deterioration directly impacts battery pole piece yield and battery consistency [22–24]. Consequently, it is imperative to study the mechanical properties and microstructural evolution of composite copper foils after long-term storage.

Based on this, this study systematically investigates the mechanical properties and microstructural evolution of composite copper foils after long-term (9-month) storage through mechanical property evaluation and microstructural analysis, while exploring the rationale of crystallographic orientation and grain size variations. The findings provide theoretical foundations for optimizing coating stress state design and developing aging-resistant composite current collectors.

## 2. Experimental

### 2.1. Materials

The materials were as follows: composite copper foil (purchased on Alibaba from Zhejiang Rouzhen Technology Co., Ltd., Haining, China), of which is a new composite copper foil named as Cu; old composite copper foil, Cu-T (storage conditions: ambient temperature at 25 degrees Celsius and ambient humidity at 40%); electrolyte (1 M LiPF<sub>6</sub> in EC:DEC:EMC = 1:1:1 by volume); sulfuric acid (H<sub>2</sub>SO<sub>4</sub>, Sinopharm Chemical Reagent Co., Ltd., AR grade, Shanghai, China); and hydrogen peroxide (H<sub>2</sub>O<sub>2</sub>, Hangzhou Bangyi Chemical Co., Ltd., AR grade, Hangzhou, China).

### 2.2. Material Characterization

Crystal structure characterization was performed using Cu K $\alpha$  radiation ( $\lambda = 1.5406 \text{ \AA}$ , 2 $\theta$  range 40–80°) via X-ray diffraction (XRD, Rigaku Ultima IV, Rigaku Corporation, Tokyo,

Japan). As shown in Figure 1, a mixed solution of 0.3 mol/L H<sub>2</sub>SO<sub>4</sub> and 0.3 mol/L H<sub>2</sub>O<sub>2</sub> was employed as the etchant to progressively thin the copper layer. Complete etching required 8 min, with etching durations of 0 min, 3 min, and 6 min corresponding to the outer layer (Cu-O), middle layer (Cu-M), and inner layer (Cu-I).

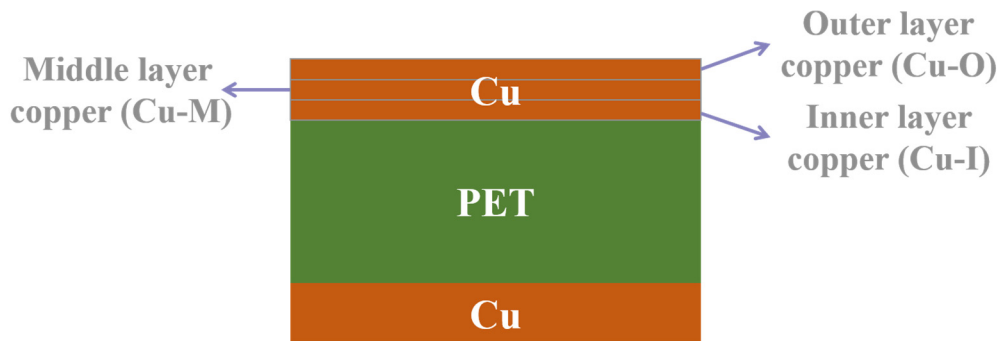


**Figure 1.** Schematic diagram of three layers for measuring XRD.

The ratio of each crystal face in copper foil can be calculated by the relative texture coefficient (RTC). The specific calculation formula is as follows:

$$RTC_{(hkl)} = \frac{I_{(hkl)}/I_{0(hkl)}}{\sum I_{(hkl)}/I_{0(hkl)}} \times 100\% \quad (1)$$

where  $RTC_{(hkl)}$  represents the RTC for the  $(hkl)$  crystal plane,  $I_{0(hkl)}$  is the diffraction intensity of the standard peak for the  $(hkl)$  plane, and  $I_{(hkl)}$  is the measured diffraction intensity of the  $(hkl)$  plane peak.

Residual stress ( $\sigma$ ) on the roughened surface of copper foil was calculated using the following equation:

$$\sigma = \frac{\varepsilon E}{2\gamma} = \frac{E(d_0 - d)}{2\gamma d} = \left(\frac{E}{4\gamma}\right) ctg \theta \times \Delta 2\theta \quad (2)$$

where  $\sigma$  represents residual stress (positive/negative values denote tensile/compressive stress),  $E$  is Young's modulus (pure copper:  $1.078 \times 10^{11}$  N·m<sup>-2</sup>),  $\gamma$  is Poisson's ratio (pure copper: 0.35), and  $d_0$  is the angular deviation of interplanar spacing from the standard reference card,  $d$  is the distance between the crystal planes.

Microstructural characterization was conducted using a field emission scanning electron microscope (FE-SEM, Thermo Scientific Apreo equipped with Oxford Ultim Max detector, Thermo Fisher Scientific, Waltham, MA, USA) integrated with an electron backscatter diffraction (EBSD) system, operating at 15 kV. Tensile strength and elongation were measured via a universal testing machine (Instron 6800 series, Instron Corporation, Boston, MA, USA). Adhesion strength between the Cu coating and PET substrate was evaluated using the cross-cut test (referencing GB/T 9286-2021). Adhesion performance was graded according to GB/T 9286-2021 criteria, where ISO Class 0 denotes the highest adhesion strength and Class 5 represents the lowest.

### 3. Results and Discussion

#### 3.1. Morphology and Tensile Properties

Figure 2a–d present the macroscopic photographs and SEM images of the Cu and Cu-T, respectively. As can be observed, both the Cu and Cu-T exhibit extremely smooth surfaces macroscopically, appearing as a relatively bright yellow-brown color. However, through SEM analysis, it can be seen that both surfaces are actually characterized by the presence of

pores and defects of various sizes, which are irregular in shape. We have calculated the holes on the surface of two kinds of composite flow collectors, and the values are, respectively, 396 per square millimeter (new composite copper foil) and 384 per square millimeter (old composite copper foil). It can be concluded that there are no significant differences between the Cu and Cu-T in terms of both macroscopic and microscopic morphologies. Figure 2e,f depict the comparison of the tensile mechanical properties of the new and aged composite copper foils. As indicated in the figures, compared to the Cu, the Cu-T shows a decline in mechanical properties, with both tensile strength and elongation rate being affected. The tensile strength decreased from the original 248.2 MPa to 224.0 MPa (a reduction of 9.76%), and the elongation rate dropped from 19% to 14% (a decrease of 26.32%). The deterioration of the mechanical properties of the composite copper foil may be detrimental to the coating and rolling processes in battery manufacturing, as well as to the stress release of the electrode during charging and discharging, thereby increasing the probability of electrode sheet fracture.

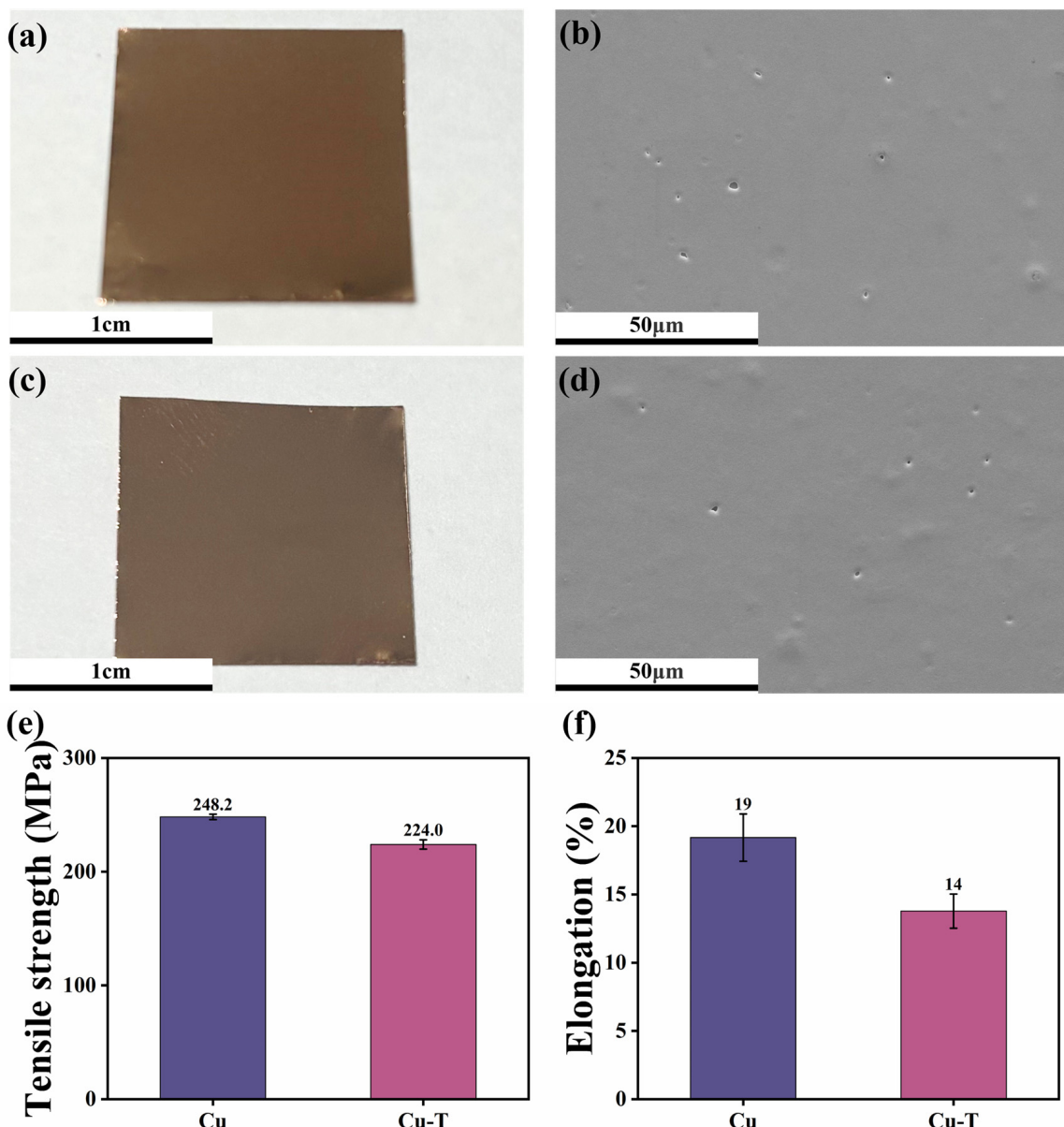


**Figure 2.** Macroscopic photos and SEM topography of Cu (a,b); macroscopic photos and SEM topography of Cu-T (c,d); tensile strength (e); and elongation (f) of Cu and Cu-T.

### 3.2. XRD Analysis

Following the methodology outlined in Figure 1, surfaces of Cu and Cu-T with varying thicknesses (as shown in Figure S1) were subjected to XRD characterization to investigate phase evolution in the copper layers. According to Formula (1), the proportion of different crystal faces was calculated. Texture coefficient calculations reveal distinct crystallographic orientation changes: in the outer layer of Cu (Cu-O), (111) planes dominate at 95.38%, with (100) and (110) planes accounting for 4.15% and <1%, respectively [25,26]. In contrast, Cu-T exhibits significantly reduced (111) orientation (64.72%), alongside increased (100) and (110) orientations (20.40% and 14.88%, respectively; in Figure 3d), demonstrating substantial reorientation during prolonged storage, marked by weakened (111) texture and strengthened (100)/(110) textures. After 3 min etching, Cu retains dominant (111) orientation (88.43%) with minor (100) (9.8%) and (110) (1.77%) contributions, while Cu-T shows drastically reduced (111) proportion (46.31%) and increased (100) and (110) fractions (23.36% and 30.33%, as shown in Figure 3b,e).

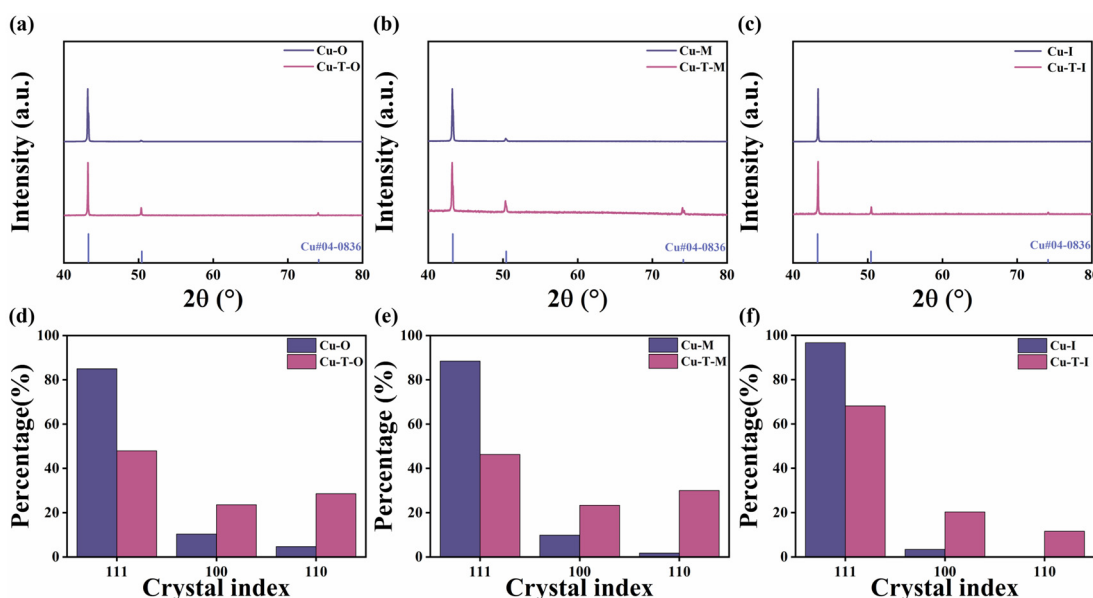


**Figure 3.** XRD patterns of different layers of Cu and Cu-T: (a) outer layer, (b) middle layer, (c) inner layer. Corresponding texture scales: (d) outer layer, (e) middle layer, (f) inner layer.

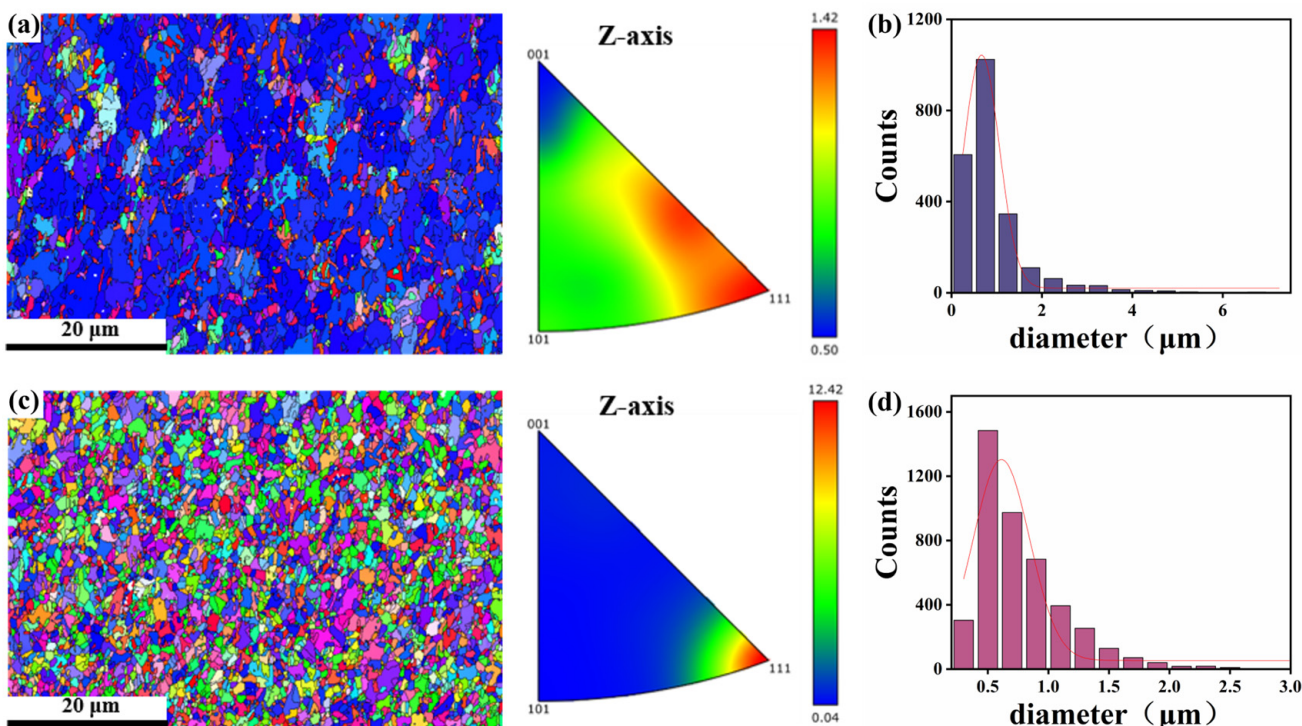
After etching for 6 min, the (111) crystal face accounted for 96.64%, (100) accounted for 3.36%. whereas Cu-T maintains a higher (111) content of 68.13%, and (100) of 20.29% and (110) of 11.58%, as shown in Figure 3c,f. These indicate that no matter in the outermost or innermost layer, the copper layer of the composite copper foil has a change in the orientation of the crystal plane, that is, the strong texture (111) is weakened and tends to disorder.

### 3.3. EBSD Analysis

#### 3.3.1. IPF Diagrams and Grain Size Analysis

To explore the reasons for the texture transformation, EBSD comparative analysis was carried out on the Cu and Cu-T, as shown in Figure 4. From the EBSD maps, it can be seen that the new composite copper foil exhibits a highly oriented (111) plane (represented by a distinct blue color), with relatively fewer (110) and (100) planes. In contrast, the aged composite copper foil shows an intermixed distribution of the three types of planes, with a relatively higher proportion of the (111) plane and fewer of the other two planes, which is consistent with the texture ratios calculated from Figure 3 XRD. As depicted in Figure 4a,b,

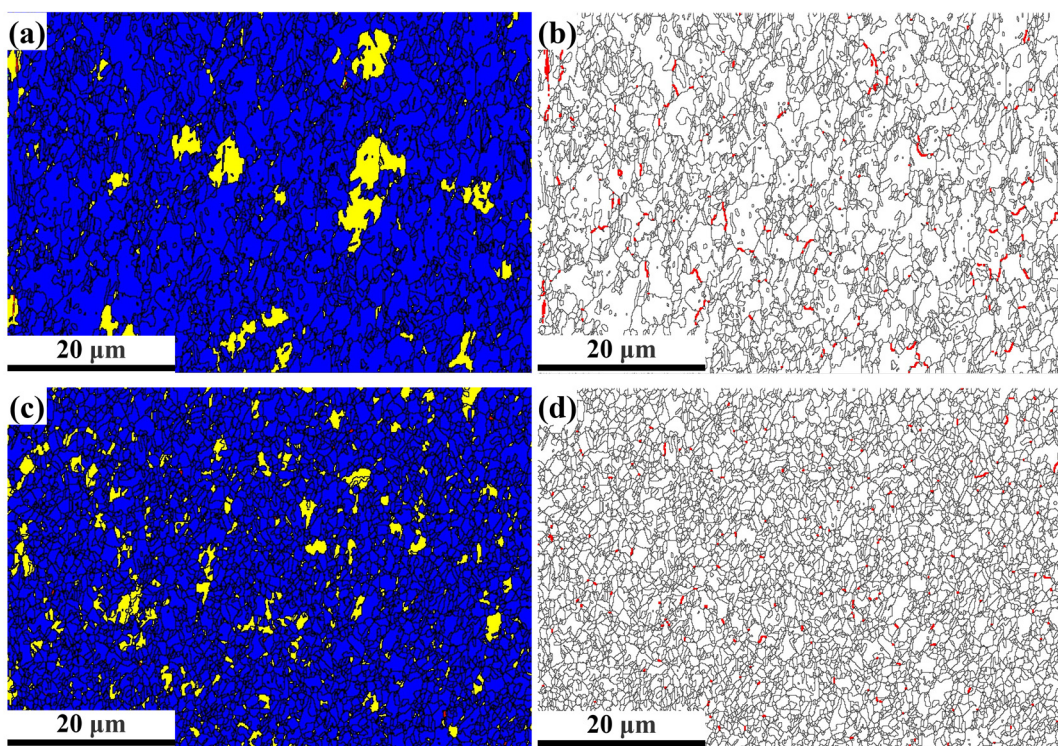
compared to the new composite copper foil, the aged one has a greater number of grains within the same area size. Through area-weighted calculations of grain size, the average grain size of the Cu-T was found to be  $1.15\text{ }\mu\text{m}$ , while that of the Cu was  $2.62\text{ }\mu\text{m}$ , indicating a significant reduction in grain size. This suggests that during the storage process, not only did the crystallographic texture undergo transformation, but the grain size also became smaller, transitioning from larger grains to smaller ones. Generally speaking, according to the fine-grain strengthening theory, the strength should have increased [27–29]. However, in reality, the Cu-T exhibited a dual decrease in tensile strength and elongation rate, indicating that the fine-grain strengthening effect was suppressed. Given the sandwich structure of the composite copper foil and the properties of each layer, it is reasonable to believe that the polymeric layer within has a significant impact on the changes in tensile strength and elongation rate [30].



**Figure 4.** EBSD diagram, Z-axis inverse pole diagram of Cu (a), grain size distribution diagram (b) EBSD diagram and Z-axis inverse pole diagram of Cu-T (c), grain size distribution diagram (d).

### 3.3.2. Recrystallization Diagrams and Size Grain Boundary Diagrams

Figure 5a,c present recrystallization diagrams of Cu and Cu-T, respectively, where blue regions denote recrystallized grains, yellow areas represent substructured grains, and red zones indicate deformed grains—all exhibiting progressively increasing dislocation densities [31]. Cu features larger yellow substructured grains with elevated dislocation content, whereas Cu-T shows fragmented substructured grains transformed into smaller blue recrystallized grains, reducing dislocation density per unit area. Figure S2 corroborates these recrystallized regions, also. Typically, increased dislocation density ( $\rho$ ) impedes dislocation motion, thereby enhancing yield strength ( $\sigma$ ) [32]. The observed dislocation reduction in Cu-T likely contributes to its diminished tensile performance [33]. Furthermore, high initial dislocation densities in Cu promote grain refinement through recrystallization-driven nucleation (accelerating grain size reduction) and texture optimization (balanced stress distribution), while facilitating the transition from low-angle to high-angle grain boundaries [34,35].



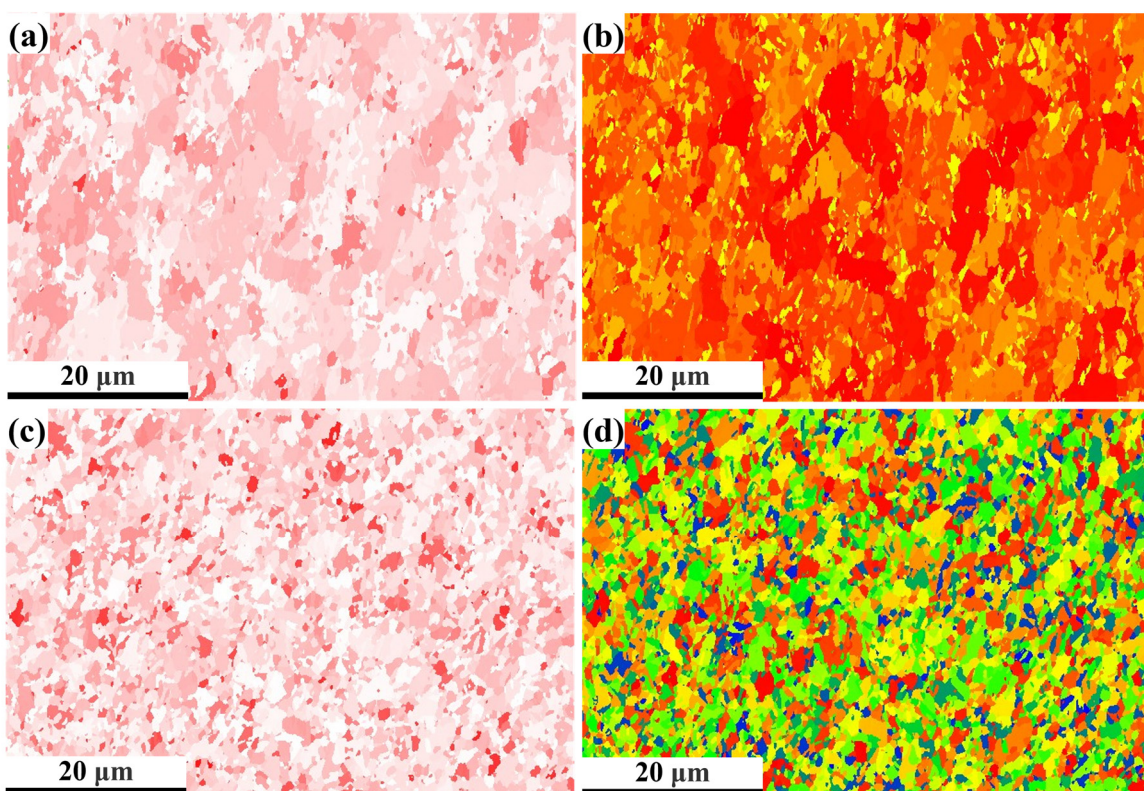
**Figure 5.** Recrystallization diagrams (a) and grain boundary diagrams (b) of Cu; recrystallization diagrams (c) and grain boundary diagrams (d) of Cu-T.

Figure 5b shows that Cu exhibits a higher density and broader distribution of low-angle grain boundaries (LAGBs, red), while Cu-T displays fewer and more dispersed LAGBs. This further confirms the transition from LAGBs to high-angle grain boundaries (HAGBs). Under elevated internal strain, increased nucleation sites in the matrix promote the formation of multiple grains [36]. These grains encounter neighboring boundaries before achieving sufficient growth, mutually inhibiting their expansion and ultimately resulting in a refined grain structure [37]. Therefore, long-term storage induces recrystallization within the composite copper foil, leading to grain size refinement. However, the expected enhancement in tensile strength due to grain refinement (via the Hall-Petch effect) is offset by the reduction in dislocation density, ultimately causing mechanical performance degradation.

### 3.3.3. Schmidt Factor and Taylor Factor

Figure 6a,c display Schmid factor diagrams for Cu and Cu-T, respectively. Color intensity correlates with Schmid factor magnitude, where lighter hues indicate easier slip system activation. Although there are more red areas inside the Cu-T (Figure 6c) compared with the Schmid factor diagram of the Cu (Figure 6a), Cu-T has more pure white layers, which indicates that the internal slip system of Cu-T is easier to slip and does not require higher stress to activate the slip. This aligns with its reduced tensile strength, consistent with prior findings. Schmidt factor diagrams can also help explain the evolution of texture. It is known that the recrystallization process occurs inside the copper layer of the composite copper foil during long-term storage, and recrystallization grains tend to nucleate in low-deformation energy storage areas, that is, in lighter colors. This can also explain that the originally large, light-colored areas of the Cu have increased grain boundaries and refined grains through recrystallization. Evolved into a small regional grain like the Cu-T. Moreover, in the long storage process, the grains of the (111) plane slip system with high Schmidt factor orientation are more prone to slip, which is controlled by the coordination

of multiple slip systems, resulting in the increase in (110) and (100) crystal faces, and the texture changes with time [38,39].



**Figure 6.** Schmid factor diagrams (a) and Taylor factor diagrams (b) of Cu; Schmid factor diagrams (c) and Taylor factor diagrams (d) of Cu-T.

The Taylor factor represents the ability of the crystal to resist plastic deformation. The comparison of the Taylor factors of the two copper foils is shown in Figure 6b,d. The redder the color in the Taylor factor diagram, the larger the Taylor factor. The larger the Taylor factor, the higher the stress required to activate the sliding system under this orientation, and the more difficult it is to activate the sliding system [40]. The smaller the Taylor factor is, the lower the stress required to activate the sliding system under this orientation, and the easier the sliding system is to activate. In the Cu, the Taylor factor is generally larger, and the grain with larger Taylor factor can withstand higher local stress, which leads to the tensile strength of the Cu is higher than that of the Cu-T. In addition, the disorderly distribution of copper grains with different sizes of Taylor factors inside the Cu-T affects the internal stress distribution, and some areas cannot withstand higher stress [41], resulting in premature rupture, reducing the tensile strength and elongation.

### 3.4. Mechanical Properties After Immersion in Electrolyte

Electrolyte immersion experiments are conducted to simulate the internal chemical/electrochemical environment of the battery, evaluate the interface stability and corrosion resistance of the composite copper foil, in order to predict its long-term service performance and avoid the risk of battery failure caused by material deterioration [42,43]. Figure 7a shows the tensile strength of Cu and Cu-T after 0, 7, and 14 days of electrolyte immersion, revealing progressive declines in both cases. Additionally, to assess the role of the intermediate PET layer, swelling mass variations in Cu and Cu-T were compared (Figure 7b). The PET swelling mass of the Cu increased by 16%, and the mass of the Cu-T increased by 15%. It shows that there is no significant difference between the amount

of absorption of PET for electrolyte, indicating that PET has a weak influence on the binding force.

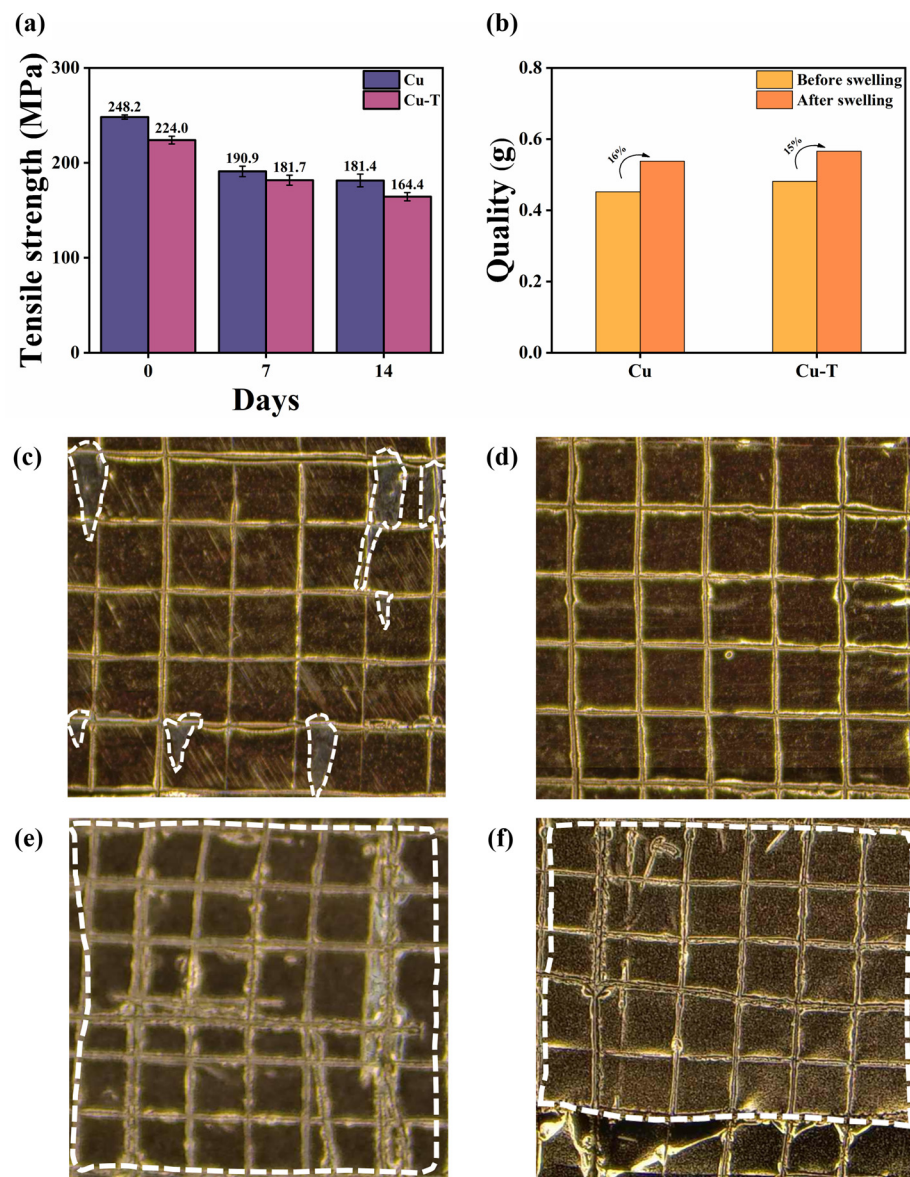


**Figure 7.** Tensile strength of Cu and Cu-T before and after electrolyte immersion (**a**), swelling mass variation in Cu and Cu-T (**b**), cross-cut test images of Cu (**c**) and Cu-T (**d**), and cross-cut test images of Cu (**e**) and Cu-T (**f**) after electrolyte immersion.

The binding force of the copper layer is judged by the scratch test of the grid knife, as shown in Figure 7c–f. There are some copper layers peeling off on the surface of Cu sample, as shown in the white dotted line Figure 7c, and a small amount of bonded copper layer is also found on the surface of the tape (as shown in Figure S3). The area of copper layer peeling off in the scribed area is less than 5%, corresponding to adhesion grades of ISO 1 or ASTM 4B [43]. In contrast, Cu-T showed no delamination, achieving superior adhesion grades of ISO 0 or ASTM 5B. This means that the bonding force between the PET layer and copper layer of the Cu is not as strong as that of the Cu-T. This phenomenon also occurs in the Cu and the Cu-T after a prolonged electrolyte immersion. After the new composite copper foil was soaked in electrolyte for a long period of time, the copper layer on the surface appeared to be completely detached from the PET layer after cleaning (as shown in Figure S4). Figure 7e,f demonstrate that the 3M tape completely peeled off the

copper layer from both foils after immersion. According to adhesion assessment criteria, the post-immersion composite copper foils (both Cu and Cu-T) exhibited adhesion grades of ISO 5 or ASTM 0B. However, the Cu-T retained partial copper layer adhesion, whereas the Cu showed no residual bonding. This further confirms the inferior interfacial adhesion strength of the Cu compared to the Cu-T.

### 3.5. Mechanism of Microstructure Evolution

Through the infrared spectrum analysis experiment (Figure 8a), it was found that there was no obvious peak generation, disappearance and migration of PET after the surface copper layer was removed from the new and old composite copper foils on the infrared spectrum. It can be shown that the PET layer between the new and old composite copper foil did not show obvious aging and degradation after long-term storage. Therefore, the source of the obvious difference between the old and new composite copper foil is not PET.

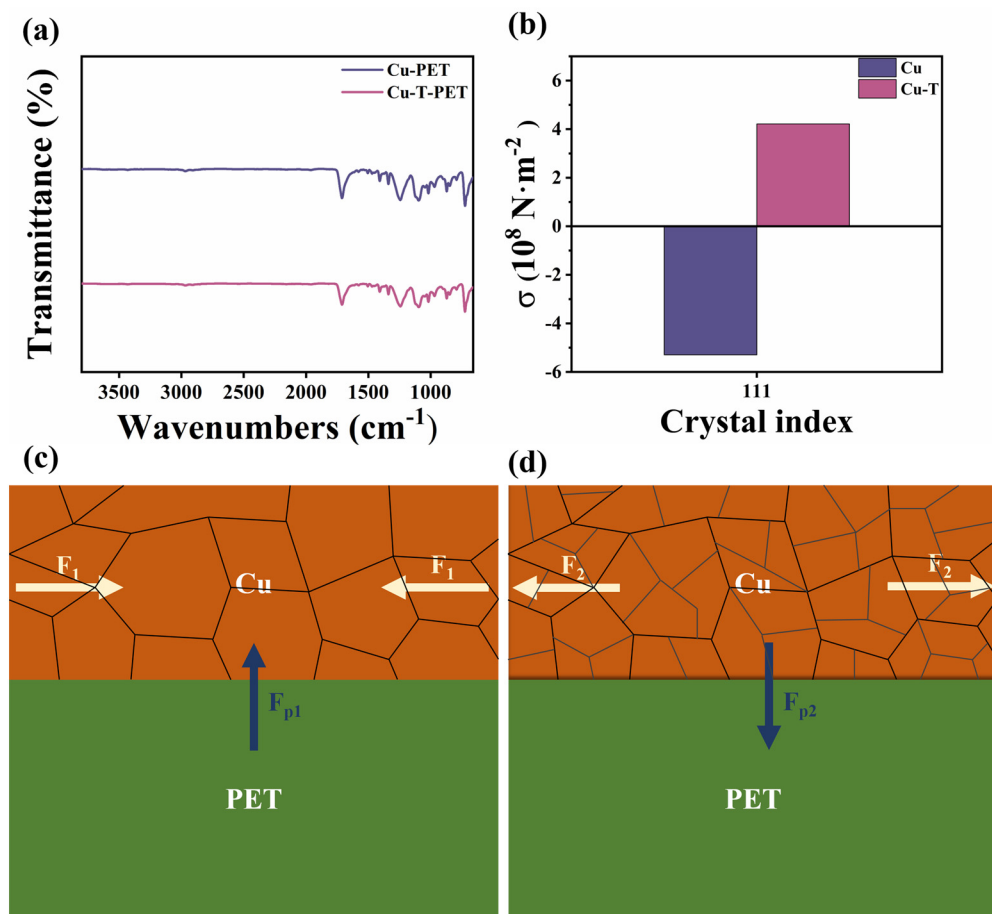


**Figure 8.** Infrared spectra of PET in the Cu and the Cu-T (a). Residual stress diagram of the Cu and the Cu-T (b). Diagram of the role of PET layer and the change process of the structure of composite copper foil (c,d).

According to the residual stress calculation formula (2), the internal residual stress of the new composite copper foil (111) is calculated as  $5.292 \times 10^8 \text{ N}\cdot\text{m}^{-2}$ , which is the compressive stress. The internal residual stress of the old composite copper foil (111) crystal face is  $4.216 \times 10^8 \text{ N}\cdot\text{m}^{-2}$ , respectively, which is the tensile stress. The energy required for the internal change in texture comes from the residual stress, and the continuous release of the residual stress causes the (111) crystal plane to transform into the (110) and (100) crystal plane with lower strain energy. It has been reported that the texture evolution of thin films is related to the interaction between surface/interface minimization and

strain energy [44–46]. When the surface/interface energy is greater than the strain energy, (111) texture predominates. Conversely, when strain energy dominates, the (100) texture dominates. Generally, electroplated copper has a stress release process after electroplating, and the release of residual stress can promote the evolution of texture and the change in grain. The initial compressive stress of the composite copper foil may be caused in part by the expansion caused by hydrogen atoms embedded in the lattice during electrolysis. After long-term storage, the residual hydrogen in the coating gradually diffuses and escapes, resulting in lattice shrinkage, and the residual stress gradually transforms into tensile stress. In addition, grain refinement may also be related to the transition of residual stress. Dislocation slip and climb driven by residual stress lead to dislocation rearrangement, forming subgrain boundaries and dividing the original large grains into smaller ones. High residual stress and defect density may reduce the recrystallization activation energy, cause local recrystallization, and destroy the initial texture. The grain boundary migrates under stress, eliminating the regions with smaller orientation difference and forming a more random grain orientation distribution [47].

The PET interlayer itself has excellent toughness, corrosion resistance and chemical stability, and plays a significant role in the entire stress release process of long-term storage. It acts as a buffer medium in the process of stress release in copper layer, regulates the redistribution of stress, and influences the microstructure evolution of copper. Under increasing stress levels, its creep compliance growth rate accelerates. According to viscoelastic theory, a material is linear viscoelastic if its creep strain remains proportional to the applied stress at any time, or if its creep compliance curves remain unchanged across different stress levels. In the process of releasing the residual stress of the copper layer on the surface of the PET substrate. PET layer played a related role in relieving stress [48], and the PET has a slow viscoelastic creep. There is a gradient of corresponding force change at the interface of the composite material, and there is a transfer process of stress from the metal layer to the substrate [49]. With the extension of time, the viscoelasticity of PET plays a role, and under the action of stress, the deformation slowly occurs, the external force is transformed into its own stress, and then the stress relaxation occurs, and the energy is dissipated.

During the preparation of composite copper foil, due to the thickening of copper deposition and the thermal mismatch effect between PET and copper, there is a high compressive stress inside the copper layer ( $F_1$  and  $F_{p1}$  in Figure 8c). During long-term storage, the residual stress in the copper layer will be gradually released [50], and the PET matrix will gradually absorb the interfacial stress through thickness compression or in-plane extension, resulting in time-dependent viscoelastic creep. This stress redistribution driven by slight creep changes the internal strain field of the copper layer, eventually exceeding its elastic recovery limit and triggering the reversal of the stress state of the copper layer from compressive stress to tensile stress ( $F_2$  and  $F_{p2}$  in Figure 8d). At the same time, the PET interface will restrict the freedom of copper grain boundary migration, promote the formation of subgrain boundaries, and destroy the stability of the initial (111) texture. In addition, the continuous viscoelastic deformation of PET may synergically reduce the activation energy of copper recrystallization, promoting grain refinement (from the recrystallization of large grains to fine grains in Figure 8c to Figure 8d) and orientation randomization.

#### 4. Conclusions

It was found that, after long-term storage, the mechanical properties of composite copper foil decrease significantly, the tensile strength decreases by 9.76%, and the elongation decreases by 28.12%. At the same time, the strong texture of (111) is significantly weakened. The variation in residual stress within the copper layer drove grain refinement and texture

randomization, while higher residual stress levels led to poorer bonding strength. Additionally, the PET layer absorbed and slowly released residual stress through creep, triggering a reversal of the stress state from compression to tension. This process, in conjunction with the synergistic effects, promoted recrystallization in the copper layer, ultimately resulting in grain refinement and randomization of orientation.

**Supplementary Materials:** The following supporting information can be downloaded at: <https://www.mdpi.com/article/10.3390/batteries11050173/s1>, Figure S1: TEM spectrum of Cu(a) and Cu-T(b); Figure S2: Overall photo of Cu and Cu-T after etching by etching fluid (left is Cu, right is Cu-T); Figure S3. GOS diagrams of new and old composite copper foils (a is Cu, b is Cu-T); Figure S4. Macroscopic photograph of the copper layer on the surface of a new composite copper foil (Cu); Figure S5. Macro-picture of the new composite copper foil (Cu) after being soaked in electrolyte and cleaned in layers.

**Author Contributions:** Conceptualization, Y.Y., J.H., J.Z., Q.C. and G.H.; Methodology, Y.Y.; Software, Y.Y. and H.L.; Validation, Y.Y.; Formal analysis, Y.Y. and H.C.; Investigation, Y.Y. and Z.X.; Resources, Y.Y.; Writing—original draft, Y.Y.; Writing—review & editing, Y.Y.; Project administration, Y.T.; Funding acquisition, Y.T. All authors have read and agreed to the published version of the manuscript.

**Funding:** This research was funded by National Natural Science Foundation of China (Grant No. 52271039, 52202315 and 52202313), “Pioneer” and “Leading Goose” R&D Program of Zhejiang, (Grant No. 2025C01182, 2023C01080), Zhejiang Provincial Natural Science Foundation of China (Grant No. LZ22E010002 and LQ22E020005).

**Data Availability Statement:** The original contributions presented in this study are included in the article and Supplementary Materials. Further inquiries can be directed to the corresponding author.

**Conflicts of Interest:** Author Ziye Xue was employed by the company Zhejiang Gpilot Technology Co., Ltd. The remaining authors declare that the research was conducted in the absence of any commercial or financial relationships that could be construed as a potential conflict of interest.

## References

- Zhang, T.; Yu, J.; Guo, H.; Qi, J.; Che, M.; Hou, M.; Jiao, P.; Zhang, Z.; Yan, Z.; Zhou, L.; et al. Sapiential Battery Systems: Beyond Traditional Electrochemical Energy. *Chem. Soc. Rev.* **2024**, *53*, 12043–12097. [[CrossRef](#)] [[PubMed](#)]
- Duan, J.; Tang, X.; Dai, H.; Yang, Y.; Wu, W.; Wei, X.; Huang, Y. Building Safe Lithium-Ion Batteries for Electric Vehicles: A Review. *Electrochim. Energy Rev.* **2020**, *3*, 1–42. [[CrossRef](#)]
- Wang, S.; Shi, J.; Liu, Z.; Xia, Y. Advanced Ether-Based Electrolytes for Lithium-ion Batteries. *Adv. Energy Mater.* **2024**, *14*, 2401526. [[CrossRef](#)]
- Shang, J.; Yu, W.; Wang, L.; Xie, C.; Xu, H.; Wang, W.; Huang, Q.; Zheng, Z. Metallic Glass-Fiber Fabrics: A New Type of Flexible, Super-Lightweight, and 3D Current Collector for Lithium Batteries. *Adv. Mater.* **2023**, *35*, e2211748. [[CrossRef](#)]
- Hao, H.; Tan, R.; Ye, C.; Low, C.T.J. Carbon-coated Current Collectors in Lithium-ion Batteries and Supercapacitors: Materials, Manufacture and Applications. *Carbon Energy* **2024**, *6*, e604. [[CrossRef](#)]
- Du, Y.; Zhang, Y.; Xue, H.; Zuo, P.; Luo, Y.; Xie, J. A Lightweight Carbon-Incorporated Polymer Current Collector for Improving the Performance and Safety of Lithium-Ion Batteries. *Carbon* **2024**, *230*, 119622. [[CrossRef](#)]
- Li, X.; Zhao, M.; Guo, Q.; Zhao, C.; Ding, M.; Zou, D.; Ding, Z.; Zhang, Z.; He, M.; Liu, K.; et al. Single-Crystallization of Electrolytic Copper Foils. *J. Mater. Sci. Technol.* **2024**, *176*, 112–118. [[CrossRef](#)]
- Zhang, J.; Zuo, D.; Pei, X.; Mu, C.; Chen, K.; Chen, Q.; Hou, G.; Tang, Y. Effects of Electrolytic Copper Foil Roughness on Lithium-Ion Battery Performance. *Metals* **2022**, *12*, 2110. [[CrossRef](#)]
- Xu, P.; Lu, W.; Song, K.; Cheng, H.; Hu, H.; Zhu, Q.; Liu, H.; Yang, X. Preparation of Electrodeposited Copper Foils with Ultrahigh Tensile Strength and Elongation: A Functionalized Ionic Liquid as the Unique Additive. *Chem. Eng. J.* **2024**, *484*, 149557. [[CrossRef](#)]
- Ouyang, Z.; Wang, S.; Wang, Y.; Muqaddas, S.; Geng, S.; Yao, Z.; Zhang, X.; Yuan, B.; Zhao, X.; Xu, Q.; et al. An Ultralight Composite Current Collector Enabling High-Energy-Density and High-Rate Anode-Free Lithium Metal Battery. *Adv. Mater.* **2024**, *36*, 2407648. [[CrossRef](#)]
- Dun, X.; Wang, M.; Shi, H.; Xie, J.; Wei, M.; Dai, L.; Jiao, S. Composite Copper Foil Current Collectors with Sandwich Structure for High-Energy Density and Safe Lithium-Ion Batteries. *Energy Storage Mater.* **2025**, *74*, 103936. [[CrossRef](#)]

12. Liao, X.; Wang, X.; Yan, C.; Zhang, B.; Ni, Y.; Yuan, H.; Pan, Y.; Pan, J.; Huang, J. Bipolar Current Collectors of Cu/Polymer/Al Composite for Anode-Free Batteries. *Adv. Funct. Mater.* **2024**, *34*, 2310925. [[CrossRef](#)]
13. Wu, X.; Chen, S.; Liu, D.; Ye, C.; Si, F.; Zhang, Y.; Yang, Y.; Luo, J.-L.; Fu, X.-Z. Polymer@Cu Composite Foils with Through-Hole Arrays as Lightweight and Flexible Current Collectors for Lithium-Ion Batteries. *J. Energy Storage* **2023**, *74*, 109208. [[CrossRef](#)]
14. Liu, Z.; Dong, Y.; Qi, X.; Wang, R.; Zhu, Z.; Yan, C.; Jiao, X.; Li, S.; Qie, L.; Li, J.; et al. Stretchable Separator/Current Collector Composite for Superior Battery Safety. *Energy Environ. Sci.* **2022**, *15*, 5313–5323. [[CrossRef](#)]
15. Ye, Y.; Chou, L.-Y.; Liu, Y.; Wang, H.; Lee, H.K.; Huang, W.; Wan, J.; Liu, K.; Zhou, G.; Yang, Y.; et al. Ultralight and Fire-Extinguishing Current Collectors for High-Energy and High-Safety Lithium-Ion Batteries. *Nat. Energy* **2020**, *5*, 786–793. [[CrossRef](#)]
16. Yang, C.H.; Yang, S.P.; Huang, B.C.; Lee, C.Y.; Liu, H.C.; Ho, C.E. In-Situ Characterization of the Microstructure Transition of Electroplating Cu during Self-Annealing and Its Effect on the Substrate Warpage. *Surf. Coat. Technol.* **2019**, *364*, 383–391. [[CrossRef](#)]
17. Yang, C.-H.; Lee, Y.-W.; Lee, C.-Y.; Lee, P.-T.; Ho, C.-E. Self-Annealing Behavior of Electroplated Cu with Different Brightener Concentrations. *J. Electrochem. Soc.* **2020**, *167*, 082514. [[CrossRef](#)]
18. Choi, J.; Hennebert, E.; Flammang, P.; Hwang, D.S. A Sugar-Lectin Rich Interface between Soft Tissue and the Stiff Byssus of *Atrina pectinata*. *Biomater. Sci.* **2020**, *8*, 3751–3759. [[CrossRef](#)]
19. Badrulin, S.I.; Noor, M.M.; Abd Samad, M.I.; Zakaria, N.S.N.; Yunas, J.; Latif, R. Eliminating Surface Cracks in Metal Film-Polymer Substrate for Reliable Flexible Piezoelectric Devices. *Eng. Sci. Technol. Int. J.* **2024**, *50*, 101617. [[CrossRef](#)]
20. Peng, Y.; Feng, X.; Xia, J.; You, Z.; Zhang, F.; Chen, Y.; Fan, C.; Hua, J.; Lian, Y.; Shan, Z.; et al. Polymer Based Multi-Layer Al Composite Current Collector Improves Battery Safety. *Chem. Eng. J.* **2024**, *491*, 151474. [[CrossRef](#)]
21. Shimizu, M.; Ohnuki, T.; Ogasawara, T.; Banno, T.; Arai, S. Electrodeposited Cu/MWCNT Composite-Film: A Potential Current Collector of Silicon-Based Negative-Electrodes for Li-Ion Batteries. *RSC Adv.* **2019**, *9*, 21939–21945. [[CrossRef](#)] [[PubMed](#)]
22. Ogata, K.; Kasuya, Y.; Gao, X.; Shibayama, Y.; Takagi, A.; Yonezu, A.; Xu, J. Adhesion Strength of an Active Material Layer/Cu Foil Interface in Silicon-Based Anodes. *ACS Appl. Mater. Interfaces* **2024**, *16*, 17692–17700. [[CrossRef](#)]
23. Li, D.; Hu, H.; Chen, B.; Lai, W. Advanced Current Collector Materials for High-Performance Lithium Metal Anodes. *Small* **2022**, *18*, 2200010. [[CrossRef](#)]
24. Feng, Y.; Fan, Y.; Zhao, L.; Yu, J.; Liao, Y.; Zhang, T.; Zhang, R.; Zhu, H.; Sun, X.; Hu, Z.; et al. Enhancing Microdomain Consistency in Polymer Electrolytes towards Sustainable Lithium Batteries. *Angew. Chem. Int. Ed.* **2025**, *64*, e202417105. [[CrossRef](#)] [[PubMed](#)]
25. Schneider, M.; Weiser, M.; Matthey, B.; Herrmann, M. In-Situ Xrd-Investigation of Electrolytic Copper Layer. *Appl. Surf. Sci.* **2018**, *457*, 815–820. [[CrossRef](#)]
26. Mao, Z.N.; Gu, R.C.; Liu, F.; Liu, Y.; Liao, X.Z.; Wang, J.T. Effect of Equal Channel Angular Pressing on the Thermal-Annealing-Induced Microstructure and Texture Evolution of Cold-Rolled Copper. *Mater. Sci. Eng. A* **2016**, *674*, 186–192. [[CrossRef](#)]
27. Fu, A.; Liu, B.; Liu, B.; Cao, Y.; Wang, J.; Liao, T.; Li, J.; Fang, Q.; Liaw, P.K.; Liu, Y. A Novel Cobalt-Free Oxide Dispersion Strengthened Medium-Entropy Alloy with Outstanding Mechanical Properties and Irradiation Resistance. *J. Mater. Sci. Technol.* **2023**, *152*, 190–200. [[CrossRef](#)]
28. Zhang, J.; Chen, H.; Fan, B.; Shan, H.; Chen, Q.; Jiang, C.; Hou, G.; Tang, Y. Study on the Relationship between Crystal Plane Orientation and Strength of Electrolytic Copper Foil. *J. Alloys Compd.* **2021**, *884*, 161044. [[CrossRef](#)]
29. Sun, J.; Jiang, T.; Wang, Y.; Guo, S.; Liu, Y. Ultrafine Grained Dual-Phase Martensite/Ferrite Steel Strengthened and Toughened by Lamella Structure. *Mater. Sci. Eng. A* **2018**, *734*, 311–317. [[CrossRef](#)]
30. Wang, H.; Guo, J.; Liu, Z. Tensile properties and failure of hybrid fiber reinforced polymer composite laminate with different fiber types, hybrid ratios, and stacking sequences. *Polym. Compos.* **2025**, *pc.29561*. [[CrossRef](#)]
31. Fan, B.; Hu, J.; Wu, Z.; Zhang, J.; Chen, Q.; Hou, G.; Tang, Y.; Hu, W. Relationship between the Orientation of the (100) Crystal Plane and Elongation in Ultrathin Electrolytic Copper Foils. *J. Phys. Chem. C* **2024**, *128*, 5759–5767. [[CrossRef](#)]
32. Li, R.; Xiao, Z.; Li, Z.; Meng, X.; Wang, X. Work Hardening Behavior and Microstructure Evolution of a Cu-Ti-Cr-Mg Alloy during Room Temperature and Cryogenic Rolling. *Materials* **2023**, *16*, 424. [[CrossRef](#)]
33. Lee, C.; Kim, Y.; Kim, R.; Yoo, B.; Kim, J.-K. Evolution of Microstructures and Mechanical Properties of Ultrahigh Strength, Pure Electrodeposited Cu during Self-Annealing. *J. Alloys Compd.* **2020**, *846*, 156488. [[CrossRef](#)]
34. Cao, X.; Zhu, Q.; Liu, Y.; Song, K.; Jia, S.; Liu, H.; Lu, W.; He, M.; Feng, Q. Grain Refinement and Texture Regulation Mechanism of Spin-Formed Commercially Pure Titanium Cathode for Electrolytic Copper Foil. *J. Mater. Res. Technol.* **2024**, *29*, 2350–2362. [[CrossRef](#)]
35. Liang, C.; Wang, N.; Chen, Y.; Jiang, C.; Wu, G.; Zhao, Q.; Zhu, L.; Luo, J. Transition of Low and High-Angle Grain Boundaries during Strain Rate-Induced Dislocation Storage and Annihilation. *Mater. Charact.* **2023**, *205*, 113284. [[CrossRef](#)]
36. Guo, B.; Gao, H.; Kong, C.; Wang, Z.; Cui, H.; Yu, H. Transverse Texture Weakening and Anisotropy Improvement of Ti-6Al-4V Alloy Sheet via Asymmetric Rolling and Static Recrystallization Annealing. *J. Alloys Compd.* **2025**, *1010*, 177507. [[CrossRef](#)]

37. Zhu, Z.; Ma, X.; Wang, C.; Mi, G. Altering Morphological, Crystalline and Compositional Features in 316 L Laser-MIG Weldments with an External Magnetic Field. *Mater. Des.* **2020**, *196*, 109156. [[CrossRef](#)]
38. Huang, L.; Dong, X.; Wei, K.; Zhang, T.; Zhang, S.; Xu, Y.; Wei, K. In-Situ Investigation of Coordinated Deformation Behavior of Ti-6242S Alloy with Duplex Microstructure. *Mater. Today Commun.* **2024**, *40*, 109813. [[CrossRef](#)]
39. Xia, Y.; Zhang, Y.; Wu, T.; Wang, N.; Ran, R.; Wang, Y.; Fang, F.; Wang, G. Deformation Twinning Caused by Warm Rolling and Secondary Recrystallization in Twin-Roll Strip Casting Fe81Ga19 Alloy. *J. Alloys Compd.* **2022**, *922*, 166039. [[CrossRef](#)]
40. Cho, C.-H.; Kim, D.-O.; Son, K.; Park, H.-S. Relationship between Hot Workability and Texture Evolution in an Al-Zn-Mg-Cu Alloy under Hot Compressive Stress Mode. *J. Mater. Sci.* **2023**, *58*, 16537–16549. [[CrossRef](#)]
41. Sarkar, A.; Sanyal, S.; Bandyopadhyay, T.K.; Mandal, S. Implications of Microstructure, Taylor Factor Distribution and Texture on Tensile Properties in a Ti-Added Fe-Mn-Al-Si-C Steel. *Mater. Sci. Eng. A* **2019**, *767*, 138402. [[CrossRef](#)]
42. Qin, G.; Zhang, J.; Chen, H.; Li, H.; Hu, J.; Chen, Q.; Hou, G.; Tang, Y. Lithium Difluoro(Oxalate)Borate as Electrolyte Additive to Form Uniform, Stable and LiF-Rich Solid Electrolyte Interphase for High Performance Lithium Ion Batteries. *Surf. Interfaces* **2024**, *48*, 104297. [[CrossRef](#)]
43. Zhang, X.; Wang, A.; Lv, R.; Luo, J. A Corrosion-Resistant Current Collector for Lithium Metal Anodes. *Energy Storage Mater.* **2019**, *18*, 199–204. [[CrossRef](#)]
44. Lin, H.-E.; Tran, D.-P.; Lin, G.-H.; Chuang, H.-J.; Chen, C. Effects of Residual Stress and Microstructure on Extremely Anisotropic Grain Growth in Nanotwinned Cu Films. *Mater. Charact.* **2024**, *211*, 113891. [[CrossRef](#)]
45. Murray, C.E.; Treger, M.; Noyan, I.C.; Rosenberg, R. Evolution of Strain Energy During Recrystallization of Plated Cu Films. *IEEE Trans. Device Mater. Reliab.* **2016**, *16*, 440–445. [[CrossRef](#)]
46. Carel, R.; Thompson, C.V.; Frost, H.J. Computer Simulation of Strain Energy Effects vs Surface and Interface Energy Effects on Grain Growth in Thin Films. *Acta Mater.* **1996**, *44*, 2479–2494. [[CrossRef](#)]
47. Du, K.; Zhang, Y.; Zhao, G.; Huang, T.; Liu, L.; Li, J.; Wang, X.; Zhang, Z. Effect of Grain Orientation and Precipitates on the Superelasticity of Fe–Ni–Co–Al Polycrystalline Alloys. *Mater. Sci. Eng. A* **2024**, *890*, 145858. [[CrossRef](#)]
48. Jung, G.; Kim, S.; Eom, J.; Song, I.Y.; Lee, J.; Cho, S.-K.; Lee, W.-E.; Heo, K.; Cho, T.-Y.; Yun, H. Substrate-dependent structural evolution during the oxidation of SiN<sub>x</sub> thin films. *J. Mater Sci.* **2024**, *59*, 10432–10443. [[CrossRef](#)]
49. Zhou, X.; Liu, S.; Amna, S.; Min, C.; Pei, X.; Liu, S.; Yin, Y.; Song, K.; Xu, Z. Construction of nanocomposite interphase with controllable thickness to relieve stress concentration and boost stress transfer from carbon fiber/epoxy resin interface. *Chem. Eng. J.* **2025**, *505*, 159542. [[CrossRef](#)]
50. Wang, L.; Bai, Z.; Sun, W.; Du, L.; Peng, X.; Xiao, Y.; Zhang, J.; Jia, Y.; Du, S.; Cai, H.; et al. Effect of Low Temperature Annealing on Microstructure and Properties of Copper Foil. *Mater. Today Commun.* **2023**, *36*, 106617. [[CrossRef](#)]

**Disclaimer/Publisher's Note:** The statements, opinions and data contained in all publications are solely those of the individual author(s) and contributor(s) and not of MDPI and/or the editor(s). MDPI and/or the editor(s) disclaim responsibility for any injury to people or property resulting from any ideas, methods, instructions or products referred to in the content.